Robust control of a floating OWC WEC under open-switch fault condition in one or in both VSCs

DIONISIO RAMIREZ, MARCOS BLANCO, MOHAMMAD EBRAHIM ZAREI, MAHIMA GUPTA

Robust control of a floating OWC WEC under open-switch fault condition in one or in both VSCs

Dionisio Ramirez[1*], Marcos Blanco[2], Mohammad Ebrahim Zarei[3], Mahima Gupta[4]

[1] Centro de Electrónica Industrial (CEI), Universidad Politécnica de Madrid, Jose Gutierrez Abascal 2, 28002 Madrid, Spain. *dionisio.ramirez@upm.es

[2] Centro de Investigaciones Energéticas, Medioambientales y Tecnológicas (CIEMAT). Av. Complutense, 40, 28040 Madrid, Spain.

[3] IMDEA Energy Institute, Electrical Systems Unit, Madrid, 28935 Spain.

[4] WEMPEC. University of Wisconsin-Madison. Engineering Hall, Room 2559. 1415 Engineering Drive. Madison, WI 53706.

Abstract: The operation and maintenance activity of off-shore wind turbines (WT) increases the cost of the generated energy. Although significant efforts have been made to improve the reliability of the mechanical subassemblies, electrical and electronic subassemblies fail more frequently, causing undesirable downtimes and loss of revenues. Since offshore WT and wave energy converters (WEC) share the electrical and electronic subassemblies, the reliability of WECs is expected to be affected by the same causes. This paper presents a robust model predictive control (MPC) for a WEC consisting of an oscillating water column (OWC) installed in a point absorber. The control system is capable of dealing with open switch faults in one or two IGBTs of the same arm in any of the voltage source converters (VSC), or even in both VSCs at the same time. The system allows the OWC WEC to generate energy, although under certain restrictions, thereby reducing the urgency of repair and loss of revenues. The performance of the proposed approach is tested for several cases of open switch faults, experimentally in the laboratory using an OWC WEC emulator.

1. Introduction

The cost of off-shore energy generation is highly impacted by the maintenance cost of the power generation system. According to some estimates [1], operation and maintenance costs account for 25-30% of energy generation from offshore wind turbines. This is primarily a result of their location, which can be tens of kilometers offshore, requiring sea or air transportation for large spare parts. Additionally, this results in significantly high downtime of the power generation unit [2]. Downtime reduces energy outputs, resulting in reduced revenue and increased expenses for the stakeholders. Therefore, it is essential to implement cost-effective operation and maintenance strategies to achieve a significant reduction in cost of energy from offshore wind farms [3].

While the industry focuses on improving the rotor blade, gearbox and other mechanical subassembly reliability using appropriate condition monitoring systems (CMS), studies indicate that electrical and electronic subassemblies also cause significant downtimes [1]. Indeed, electrical and electronic subassemblies fail more frequently than mechanical ones, although the mechanical subassemblies experience longer downtimes. Minor failures in electrical system result in the gearbox and the rotor downtime of eight and two times, respectively [1]. Among the failures related to the electronic subassembly, those related to the power converter account for almost half (48%) of the failures in the electrical system of the wind turbines [2]. Thus, to improve the wind turbines' availability, operators can attend to minor failures, particularly due to electrical and electronic subassemblies. WECs share similar problems of reliability since they are also located offshore and share the same electrical, electronic and control subassemblies as wind turbines.

Although, the reliability of WECs has not been greatly studied, the knowledge obtained from off-shore wind turbines is useful. For example, it is expected that OWCs include conditioning monitoring technology [3] for analyzing the electrical signals of WEC. However, only the standard/TS IEC TS 62600-2 is dedicated specifically to the design of marine energy converters which gives design guidance for current energy converters (CECs), tidal energy converters (TECs) and WECs.

Fault-tolerant control (FTC) systems are generally split into active (AFTC) and passive fault-tolerant (PFTC) structures [4]. AFTC systems [5] contain three layers: the first layer is related to the inner control loop; the second layer corresponds to the fault detection, isolation, and accommodation modules; and the last layer corresponds to the supervisor system. The system proposed in this paper belongs to the first layer of the AFTC and it is intended to improve the reliability of a WEC in order to reduce the downtime when a fault takes place in one or up to two switches of the same arm of any of the VSCs, either machine side converter (MSC) or grid side converter (GSC), or even in both VSCs at the same time. Thus, the electronic converter can keep working, although under some restrictions, extracting energy from the WEC and sending it to the grid. This reduces the downtime, the urgency for the repair team to reach the WEC and to carry out the repair, and keeps the WEC generating profits, reducing the average cost of the generated energy.

Although several approaches have been proposed to keep a VSC connected and operational when an IGBT breaks down, the DC bus midpoint connection to the three-legs via TRIACs is the most widely accepted solution [6]. However, keeping the power converter working requires the development of specific control strategies for post-fault operation. An approach based on a two-vector modeless predictive controller is presented in [7] where a good tracking of the

current reference is achieved but the accuracy of the predictions is a function of the sampling rate and the accuracy of the sensors. In [8] a fast algorithm capable to find the three vectors that minimize the cost function of the MPC in just one step is presented, avoiding searching the location of the reference vector or assessing all the pairs of adjacent vectors in the cost function which reduces significatively the computing time.

Modulation is another key aspect of open switch fault tolerant systems since the number of available vectors to carry out the modulation after the fault is only four. For example, in [9] the duty cycles of the vectors are calculated by means of simple equations, which, although gives rise to a simple modulation, makes it unnecessary to find the sector where the voltage reference is located. The modulation proposed in [10] is simple to implement and uses the smallest vectors to generate the zero vector which improves the performance. In addition, a DC voltage offset suppression method is proposed which maximize the utilization of the DC -bus voltage. In [8] is proposed a modulation system specifically designed for open switch faults which rebuilds the hexagon from the four remaining vectors and that features short cycle time, constant switching frequency and three vectors per PWM period, low ripple in the currents and fast dynamic response.

The control system used in this paper develops the MPC and modulation presented in [8] and analyzes the different challenging situations faced by each VSC after a fault as well as the new limits of power and speed of the Wells turbine and relates them the OWC air chamber control.

The paper is organized as follows. Section 2 presents the mathematical model of the OWC WEC. In Section 3, the proposed dual open switch fault tolerant MPC for the floating OWC is presented. In Section 4 the calculation of the reference voltage vector and the modulation are explained. Section 5 describes the OWC WEC emulator and the experimental tests carried out in the laboratory. Finally, in Section 6 the conclusions obtained are presented.

2. Mathematical model of the emulated OWC WEC

The OWC WEC is a type of wave energy converter, which features an internal air chamber and an oscillating water column within a rigid exterior hull. When perturbed by sea waves, the relative motion between the free surface of the water column and the rigid hull creates a differential pressure between the air chamber and the external environment. This differential pressure drives an air flow across an air turbine, in turn, providing mechanical power to a rotating generator. The rigid hull can either be fixed to the shoreline or can be floating, like in the case considered in this paper [11].

The axisymmetric-type OWC WEC modeled in this paper, Fig. 1, consists of a submerged vertical tube, open at both ends, which is fixed to a floater that moves in a heave [12]. This device is modeled as a 2-body device: the point absorber composed of a floater and a tail tube (body 1) and the water inside the chamber, modelled as an weightless rigid piston (body 2) (assuming that the OWC diameter is much smaller than the wave length [13]). The nomenclature of the model and the dimensions are shown in Table 1 and Table 2 respectively. The block diagram of the emulator is presented in Section 5.
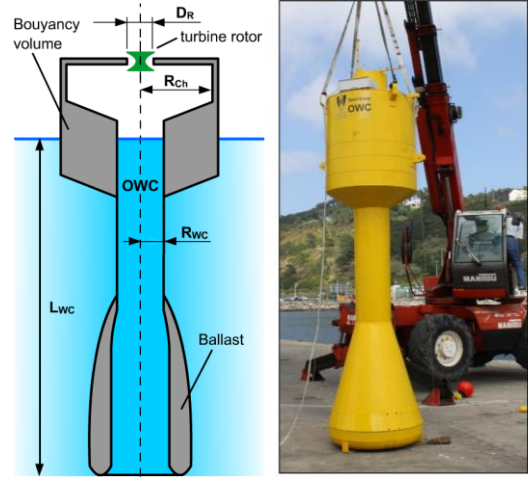
Fig. 1. *Scheme (left) and photography (right) of an floating OWC WEC* [12]

2.1. OWC Point absorber model

The 2-body dynamic system is characterized by second Newton's Law. By choosing an inertial reference frame, the dynamic time-domain equations, in Laplace domain, results in (1)-(2) for body 1 and body 2, respectively [14].

$$(m_1 + M_{11}^\infty) \cdot s \cdot u_1(s) + \varrho_w \cdot g \cdot S_1 \cdot \frac{u_1(s)}{s} + M_{12}^\infty \cdot s \cdot u_2(s) + R_{11} * \dot{x}_1 + R_{12} * \dot{x}_2 = F_{e,1} + F_{PTO} \quad (1)$$

$$(m_2 + M_{22}^\infty) \cdot s \cdot u_2(s) + \varrho_w \cdot g \cdot S_2 \cdot \frac{u_2(s)}{s} + M_{21}^\infty \cdot s \cdot u_1(s) + R_{22} * \dot{x}_2 + R_{21} * \dot{x}_1 = F_{e,2} - F_{PTO} \quad (2)$$

The coefficients in (1)-(2) are determined by analyzing the physical geometry of the point absorber in WaveAnalysisMIT (WAMIT) program. WAMIT utilizes boundary element method (BEM) to analyze floating and submerged bodies in the presence of ocean waves.

This model is obtained by the summation of all the forces that act on each body [13][15] where only the heave (vertical) motion of the bodies has been considered in the analysis. Equations (1)-(2) consider buoyancy forces, hydrodynamics radiation forces, hydrodynamic excitation forces and PTO forces. The PTO force can be expressed in terms of the pressure in the air chamber; and this variable is related with the Wells turbine variables (specifically with the rotation speed). These relationships are discussed in the following sections.

2.2. Air chamber/Wells turbine model

Considering that the air inside the chamber is an isentropic fluid, the linearized relation between the air density and the air pressure is given by (3).

$$\dot{\rho} = \frac{\rho_0}{\gamma \cdot p_0} \cdot \dot{p} \quad (3)$$

The air mass flow through the Wells turbine (4) can be obtained from (3),

$$\dot{m} = -\frac{d}{dt}(\rho \cdot V) = -\frac{\rho_0 \cdot V_0}{\gamma \cdot p_0} \cdot \dot{p} - \rho_0 \cdot S_2 \cdot (\dot{x}_1 - \dot{x}_2) = -\frac{\rho_0 \cdot V_0}{\gamma \cdot p_0} \cdot \dot{p} - \rho_0 \cdot S_2 \cdot u_r \quad (4)$$

2

where, V represents the volume of the air inside the chamber i.e. $V = V_0 + (x_1 - x_2) \cdot S_2$ and u_r is the relative speed between the point absorber and the water column.

Assuming a Wells turbine, k_t^* [16] can be established to be a linear ratio of the relative pressure, Ψ, and the relative flow Φ by (5)

$$k_t^* = \frac{\Psi}{\Phi} = \frac{D \cdot p}{\dot{m} \cdot N} \tag{5}$$

where,

$$\Psi = \frac{p}{\rho_0 \cdot N^2 \cdot D^2}; \qquad \Phi = \frac{\dot{m}}{\rho_0 \cdot N \cdot D^3} \tag{6}$$

Hence, the mass flow equation (4) can be reduced to (7).

$$\dot{m} = \frac{D \cdot p}{k_t^* \cdot N} \tag{7}$$

Finally, using Eq. (4) and Eq. (7), the air pressure can be obtained in Laplace domain (8)

$$p(s) = \frac{\varepsilon \cdot u_r(s)}{1 + \varepsilon \cdot \Gamma \cdot s}; \quad \varepsilon = \frac{L_0}{\gamma \cdot p_0}; \quad \Gamma = \frac{\rho_0 \cdot S_2 \cdot N \cdot k_t^*}{D} \tag{8}$$

The force imposed by the PTO can be expressed, in the frequency domain, in terms of the relative speed as:

$$\hat{F}_{PTO} = S_2 \cdot \hat{p} = -i \cdot \frac{K_{PTO}}{\omega} \cdot \hat{u}_r - B_{PTO} \cdot \hat{u}_r;$$
$$K_{PTO} = \frac{S_2 \cdot \varepsilon \cdot \Gamma^2}{1 + (\omega \cdot \varepsilon \cdot \Gamma)^2}; \quad B_{PTO} = \frac{S_2 \cdot \Gamma}{1 + (\omega \cdot \varepsilon \cdot \Gamma)^2} \tag{9}$$

2.3. Power extracted evaluation

Finally, in order to evaluate the power extracted by the OWC and the torque, it is necessary to include the Wells turbine model. The relation between the relative power, Π, and the relative pressure, Ψ, is shown in Fig. 2 and is programmed as a look-up table in the MCU.
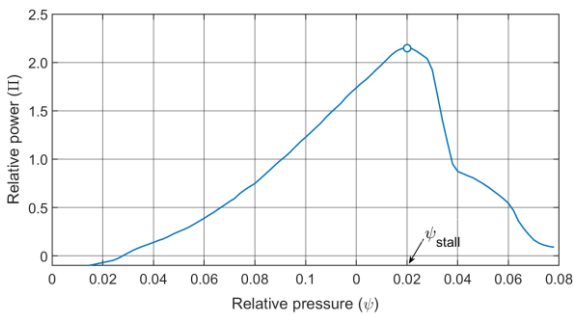
Fig. 2. Relative power, Π, of the Wells turbine vs. relative pressure, Ψ, of the air across the turbine

The input to this table, Ψ, is calculated using Eq. (5) and the result, Π, using Eq. (10) allows obtaining the PTO power.

$$\Pi = \frac{P}{\rho_0 \cdot N^3 \cdot D^5} \tag{10}$$
$$T_{PTO} = \Pi \cdot \rho_0 \cdot N^2 \cdot D^5 \tag{11}$$

3. Post fault topology

After the open switch fault is detected in one or two IGBTs of the same-leg in the MSC or the GSC, the corresponding faulty phase is connected to the mid-point of the DC bus. Once the post-fault configuration is adopted, the VSC is capable of generating a limited set of space vectors, Table 3. The AC phase connected to the capacitors produces variations on the capacitor voltages hence, $vc1 \neq vc2$. Consequently, according to Table 3, the magnitude and phase of the space vectors generated by the VSCs are not constant [17]. Also, the rated power of the VSC after the fault is approximately half of the pre-fault rating since the maximum magnitude of the output voltage vector is now lower. The effective V_{DC} after the fault, considering the capacitor voltages are similar, is defined by the relationship between the $\vec{v}_{ref}$ magnitudes before and after the fault

$$\frac{|\vec{v}_{ref}| \, after \, fault}{|\vec{v}_{ref}| \, before \, fault} = \frac{\frac{V_{DC}/2}{\sqrt{3}}}{\frac{2}{3} \cdot V_{DC} \cdot cos30^0} = \frac{1}{2} = \frac{V_{DC} \, after \, fault}{V_{DC} \, pre \, fault} \tag{12}$$

However, if the capacitor voltages are not balanced, the effective V_{DC} is the minimum of $vc1$ and $vc2$ [18].

Another consequence of the fault is that it might be necessary for the VSC to absorb a certain amount of reactive power when its output voltage is lower than that of the AC source to which it is connected. That is described in detail in the following subsection Section 3.1.

Depending on the location of the fault in the VSC, three different topologies are possible, as shown in Fig. 3.

3.1. Open switch fault in the GSC

In Fig. 3 (top), the phase "a" of the grid connection has been connected to the midpoint of the DC bus. This VSC is able to generate the space vectors of Table 3 whereas the MSC is able to generate a full hexagon of space vectors. In this case, the GSC is responsible for keeping V_{DC} constant for both VSCs despite the fault.

However, the power that can be obtained from the OWC WEC is now limited by the new GSC rated power (which approximately half of the pre-fault value). Therefore, it is necessary to limit the OWC WEC output power by opening the relief valve in the air chamber to limit the relative pressure, Ψ, although this control is not very accurate [16][19]. Another possibility is increasing the rated current of IGBTs of the GSC to compensate for the limited output voltage with an increment of the line currents. However, the ideal would be combining both systems to limit the overrating of the IGBTs and other components such as inductors, transformer windings, etc. In addition, it is likely that the GSC needs to absorb reactive power [18] due to the low effective V_{DC} (the lowest between $vc1$ and $vc2$).

The post-fault limits of power can be analyzed by means of the circumferences of maximum output voltage, $\vec{v}_{ref\,max}$, and of IGBTs rated current, $\vec{I}_{max}$, in a plane [18] where the vertical and horizontal axes are proportional, to the active power and reactive power, respectively, exchanged between the VSC and the grid. In the graph of powers represented in Fig. 4, the permitted operation area (where $|\vec{v}_{ref}| < |\vec{v}_{ref\,max}|$ and $|\vec{I}| < |\vec{I}_{max}|$) has been colored in gray and three operation points have been represented. The first case represents the maximum power, P that the GSC is capable of exchanging

with the grid, which corresponds to the maximum magnitude of $\vec{v}_{\text{ref}}$. In the following case, the magnitude of $\vec{v}_{\text{ref}}$ and P have intermediate values, and in the last case, $\vec{v}_{\text{ref}}$ is horizontal and P=0.
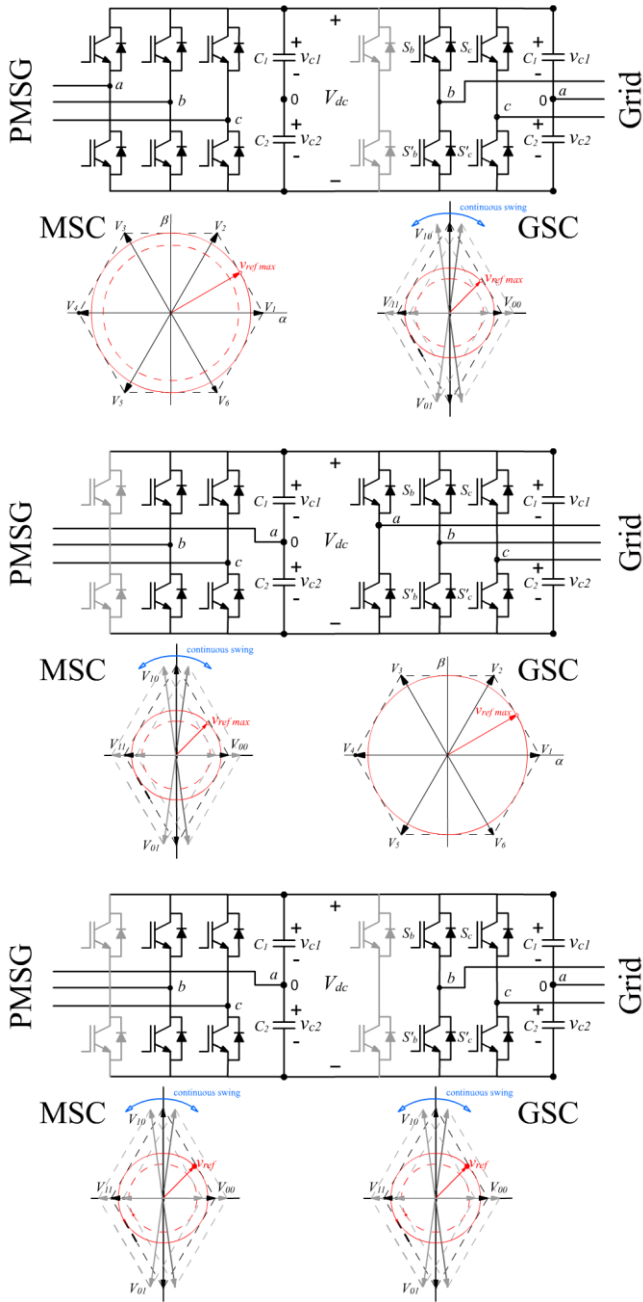
Fig. 3. *Post-fault topology and space vectors: top) fault in the GSC; middle) fault in the MSC; bottom) fault in GSC and MSC*

Note that in all cases, Q<0, hence the GSC is absorbing reactive power from the grid. This is necessary to keep the operation point inside the gray area, and it is a consequence of the low value of the magnitude of $\vec{v}_{\text{ref}}$ compared to that of $\vec{v}_{\text{grid}}$, and ultimately a consequence of the low effective V_{DC} after the fault. By observing Fig. 4, it is obvious that this issue can be reduced by increasing the DC link voltage after the fault (it increases $|\vec{v}_{\text{ref}}|$ and the red circumference radius) or by reducing the grid voltage using a tapped transformer (reducing $|\vec{v}_{\text{grid}}|$).
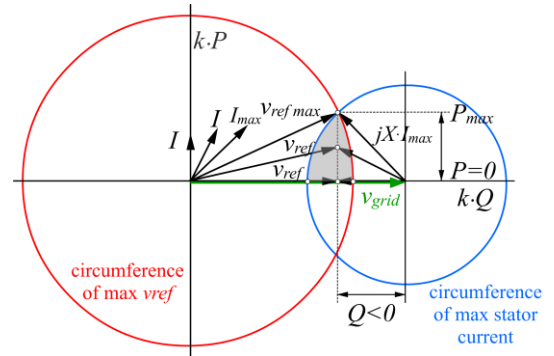
Fig. 4. *Diagram of active and reactive powers of the GSC.*
$$k = (2/3) \cdot \left(X/V_{grid} \right).$$

3.2. Open switch fault in the MSC

In the case of an open switch fault in the MSC, represented in Fig. 3 (middle), two limits coexist:

a) The MSC rated power during the fault is lower than the pre-fault power since the effective V_{DC} is the minimum of $vc1$ and $vc2$, that limits its output voltage, even though the rated current is not affected. The incoming power to the PMSG can be limited, as described section 3.1, by opening the relief valve of the air chamber.

b) The e.m.f. of the PMSG is limited by the new value of the MSC maximum output voltage since, otherwise, the MSC and the PMSG cannot exchange power. In effect, as the e.m.f. of PMSG increases with the rotor speed, the maximum active power that the MSC is capable to handle decreases, Fig. 5a and Fig. 5b, although it is still capable to provide reactive power to the internal reactance of the generator ($k \cdot Q > 0$). However, a moment comes, Fig. 5c, when the rotor speed, and therefore the e.m.f., restricts the MSC to exchange the active and reactive power with the PMSG. Indeed, although in b) the MSC is feeding the internal inductance of the PMSG with reactive power, it is no longer capable of handling the mechanical torque generated by the turbine, so the rotor speed will increase, and the control of the generator will be lost. Therefore, the e.m.f. must be limited to approximately half its rated value by limiting the rotor speed through load torque generated by the MSC (the e.m.f. is proportional to ω). However, limiting the rotor speed has the side effect of increasing the phase currents since the load torque is controlled through i_{sq}. If the current reaches the rated value of the PMSG windings and IGBTs, the turbine power must be limited by opening the relief valve further. An alternative could be to increase the IGBTs rated current, but it implies overrating the PMSG stator windings which is not practical since it means increasing the generator rated power and its cost.
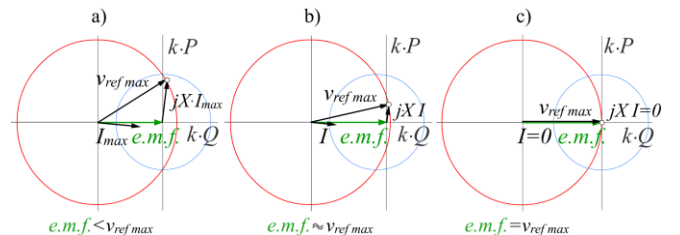
Fig. 5. *Diagram of active and reactive powers of the MSC in three different cases.*

The MSC should not absorb reactive power from the PMSG to avoid weakening the field of the rotor magnets which limits the MSC range of operation points more than in the GSC case, where absorbing reactive power is not a problem. In this case, it could be advisable to overrate the IGBT emitter-collector voltage to increase V_{DC} after the fault in order to keep, to some extent, the MSC rated output voltage and the rated power. A rule of thumb could be that $V_{DC}/2$ is at least 1.5 times higher than the peak e.m.f. to allow an acceptable handling of the turbine power and torque.

3.3. Open switch fault in the MSC and the GSC

This case corresponds to a double fault, one in each VSC, Fig. 3 (bottom). The GSC is responsible for keeping V_{DC} constant for both VSCs and the MSC limits the rotor speed to half the rated one, and the OWC WEC power and phase current through the relief valve in the air chamber. The post-fault rated power is the same in both VSCs. Each VSC handles $vc1$ and $vc2$ with its own DC offset suppression method.

4. Control systems

The control systems used to obtain the maximum power from the waves are both, in the machine side converter (MSC) and in the grid side converter (GSC), Model Predictive Controls although they use different reference frames.

4.1. MSC predictive control

Extracting the maximum power from the waves means that the torque of the electric generator must be controlled following a certain strategy that maximizes the power exchange between the Wells turbine and the generator. Model predictive control of a PMSG is based on its electric model (see Table 4 for nomenclature). The electric equations of a PMSG expressed in the rotor rotating reference frame, d-q frame, are

$$v_{sd} = R_s i_{sd} + \frac{d}{dt}\lambda_{sd} - \omega_m \lambda_{sq} \tag{15}$$

$$v_{sq} = R_s i_{sq} + \frac{d}{dt}\lambda_{sq} + \omega_r \lambda_{sd} \tag{16}$$

As it is described in [20], by calculating the slopes of i_{sd} and i_{sq}, $S_{i_{sd}}$ and $S_{i_{sd}}$ caused in the current by space vectors, $\vec{v}_a, \vec{v}_b, \vec{v}_c$ that the electronic converter applies in a fixed sequence. Denoting $i_{sd}(k)$ to the value of the current at the end of the previous cycle, after the application of the three space vectors in the current switching period, the stator current is

$$i_{sd}(k + 1) = i_{sd}(k) + S_{da}t_a + S_{db}t_b + S_{dc}t_c \tag{17}$$

$$i_{sq}(k + 1) = i_{sq}(k) + S_{qa}t_a + S_{qb}t_b + S_{qc}t_c \tag{18}$$

The objective is to obtain a good i_{sd} and i_{sd} reference tracking, hence the cost function to minimize can be represented as

$$F(k + 1) = \left(i_{sd}(k + 1) - i_{sd}^*(k)\right)^2 + \left(i_{sq}(k + 1) - i_{sq}^*(k)\right)^2 \tag{19}$$

where, the superscript * denotes the reference values. After minimizing (19), the duration times for each voltage vector within a switching interval result in [20]

$$t_a = \frac{\left(i_{sd}(k)-i_{sd}^*(k)\right)\cdot(S_{qc}-S_{qa})+\left(i_{sq}(k)-i_{sq}^*(k)\right)\cdot(S_{da}-S_{dc})+T_s(S_{qc}\cdot S_{da}-S_{qa}\cdot S_{dc})}{S_{qa}(S_{db}-S_{dc})+S_{qb}(S_{dc}-S_{da})+S_{qc}(S_{da}-S_{db})} \tag{20}$$

$$t_b = \frac{\left(i_{sd}(k)-i_{sd}^*(k)\right)\cdot(S_{qa}-S_{qb})+\left(i_{sq}(k)-i_{sq}^*(k)\right)\cdot(S_{db}-S_{da})+T_s(S_{qa}\cdot S_{db}-S_{qb}\cdot S_{da})}{S_{qa}(S_{db}-S_{dc})+S_{qb}(S_{dc}-S_{da})+S_{qc}(S_{da}-S_{db})} \tag{21}$$

$$t_c = T_s - t_a - t_b \tag{22}$$

Finally, the reference voltage vector, $\vec{v}_{ref}$, in the stationary reference frame can be written as follows

$$\vec{v}_{ref} = v_{ref\alpha} + jv_{ref\beta} = \vec{v}_a \cdot \frac{t_a}{T_s} + \vec{v}_b \cdot \frac{t_b}{T_s} + \vec{v}_c \cdot \frac{t_c}{T_s} \tag{23}$$

independently of which vectors, $\vec{v}_a, \vec{v}_b$, and $\vec{v}_c$, are applied to the stator.

4.2. GSC predictive control

The relationship between the GSC voltage and the grid voltage in the stationary reference frame is (see Table 5 for nomenclature)

$$\vec{v}_{GSC} = \vec{v}_g + L_f \frac{d\vec{i}_g}{dt} + R_f \vec{i}_g \tag{24}$$

The active and reactive powers exchanged by the GSC and the grid can be calculated as

$$P_g = 1.5 \cdot \left(v_{g\alpha}i_{g\alpha} + v_{g\beta}i_{g\beta}\right) \tag{25}$$

$$Q_g = 1.5 \cdot \left(v_{g\beta}i_{g\alpha} - v_{g\alpha}i_{g\beta}\right) \tag{26}$$

As explained in [21][8], it is possible to obtain the power value at the end of the current switching cycle (instant k+1) if the effect on the power of all the voltage vectors successively applied by the GSC is added to the power value at the beginning of the cycle (instant k),

$$P_g(k + 1) = P_g(k) + S_{Pa}t_a + S_{Pb}t_b + S_{Pc}t_c \tag{27}$$

$$Q_g(k + 1) = Q_g(k) + S_{Qa}t_a + S_{Qb}t_b + S_{Qc}t_c \tag{28}$$

where the power slopes, S_{Pi}, S_{Qi}, for each voltage vector must be calculated as explained in [21].

The cost function used to obtain a good tracking of the power references is

$$F(k + 1) = \left(Q_g(k + 1) - Q_g^*(k)\right)^2 + \left(P_g(k + 1) - P_g^*(k)\right)^2 \tag{29}$$

By minimizing this function, the duration times of each vector result

$$t_a = \frac{\left(P_g(k)-P_g^*(k)\right)\cdot(S_{Qa}-S_{Qb})+\left(Q_g(k)-Q_g^*(k)\right)\cdot(S_{Pb}-S_{Pa})}{S_{Q0}(S_{Pa}-S_{Pb})+S_{Qa}(S_{Pb}-S_{P0})+S_{Qb}(S_{P0}-S_{Pa})}+$$
$$\frac{T_s(S_{Qa}\cdot S_{Pb}-S_{Qc}\cdot S_{Pa})}{S_{Q0}(S_{Pa}-S_{Pb})+S_{Qj}(S_{Pb}-S_{P0})+S_{Qb}(S_{P0}-S_{Pa})} \tag{30}$$

$$t_b = \frac{\left(P_g(k)-P_g^*(k)\right)\cdot(S_{Qb}-S_{Q0})+\left(Q_g(k)-Q_g^*(k)\right)\cdot(S_{P0}-S_{Pb})}{S_{Q0}(S_{Pa}-S_{Pb})+S_{Qj}(S_{Pb}-S_{P0})+S_{Qb}(S_{P0}-S_{Pa})}+$$
$$\frac{T_s(S_{Qb}\cdot S_{P0}-S_{Q0}\cdot S_{Pb})}{S_{Q0}(S_{Pa}-S_{Pb})+S_{Qj}(S_{Pb}-S_{P0})+S_{Qb}(S_{P0}-S_{Pa})} \tag{31}$$

$$t_c = T_s - t_a - t_b \tag{32}$$

Finally, the reference voltage vector, $\vec{v}_{ref}$, expressed by its α-β coordinates, is

$$\vec{v}_{ref} = v_{ref\alpha} + jv_{ref\beta} = \vec{v}_a \cdot \frac{t_a}{T_s} + \vec{v}_b \cdot \frac{t_b}{T_s} + \vec{v}_c \cdot \frac{t_c}{T_s} \tag{33}$$

The next step in both MPCs (MSC and GSC) is to reproduce $\vec{v}_{ref}$ by means of modulation. The vectors used to carry out the modulation must be those that minimize the cost function. A fast method consists of using $\vec{V}_1$, $\vec{V}_2$ and $\vec{V}_0$ for all the sectors, Fig. 6, since $\vec{v}_{ref}$ can be expressed as a combination of $\vec{V}_1$, $\vec{V}_2$ and $\vec{V}_0$ in any sector [8]. The result obtained for $\vec{v}_{ref}$ is valid but not the duration times, that are sporadically negative or greater than 1. However, a standard SVM can carry out the modulation from the values of $v_{ref\alpha}$ and $v_{ref\beta}$.

4.3. Modulation

Once the open-switch fault takes place, the number of available space vectors is reduced to four wherein, they have a different magnitude and, if $vc1 = vc2$, the angle between them is 90º. However, it is possible to obtain a regular hexagon defined by six space vectors from the four remaining space vectors, $\vec{V}_{00}, \vec{V}_{01}, \vec{V}_{10}$ and $\vec{V}_{11}$, as Fig. 7 shows [8]. For example, $\vec{V}_2$ can be reproduced by averaging $\vec{V}_{00}$ and $\vec{V}_{10}$.

$$\vec{V}_2 = \left(\frac{V_{DC}}{3}\right)_{|60^0} = \vec{V}_{00} \cdot d_{V00} + \vec{V}_{10} \cdot d_{V10} \tag{34}$$

where, d_{V00} and d_{V00} are the duty cycles.

When $vc1 = vc2$, the duty cycles result in

$$d_{V00} = \frac{3}{2} \cdot \frac{|v_{ref\alpha}|}{V_{DC}} = \frac{1}{2} \quad \text{and} \quad d_{V10} = \frac{\sqrt{3}}{2} \cdot \frac{|v_{ref\beta}|}{V_{DC}} = \frac{1}{2} \tag{35}$$

This result can be generalized for $\vec{V}_2, \vec{V}_3, \vec{V}_5$ and $\vec{V}_6$.

The resulting hexagon, Fig. 7, is smaller than that before the fault but, once built, it can be used as a standard SVM [8].

The combination of rebuilding the hexagon and using it to carry out a standard space vector modulation results in the product of two modulations. For example, vectors V_{00}, V_{10} are used to reproduce $\vec{V}_2$, and V_{00} to reproduce $\vec{V}_1$, using the first modulation. But at the same time, $\vec{V}_1$ and $\vec{V}_2$ are used by the SVM to reproduce any $\vec{v}_{ref}$ located within Sector I, which leads to a second modulation. Thus, in Sector I, $\vec{v}_{ref}$ is calculated using the duty cycles, d_{V_1} and d_{V_2}
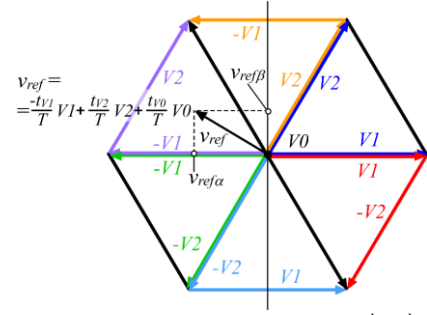
Fig. 6. $\vec{v}_{ref}$ expressed as a combination of $\vec{V}_1$, $\vec{V}_2$ and $\vec{V}_0$
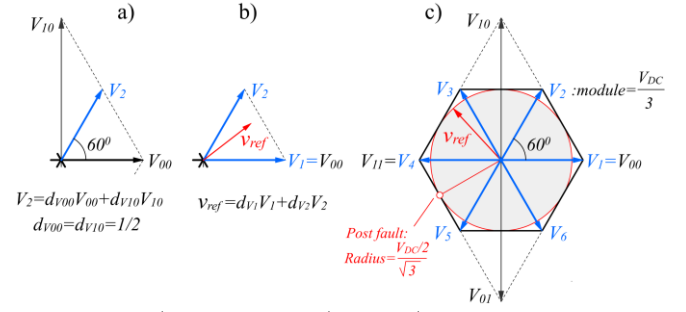
Fig. 7. a) $\vec{V}_2$ rebuilt from $\vec{V}_{00}$ and $\vec{V}_{10}$; b) $\vec{v}_{ref}$ obtained from the rebuilt $\vec{V}_2$ and $\vec{V}_1$; c) using the rebuilt hexagon it is possible to modulate $\vec{v}_{ref}$ in any location within the circumference.

$$\vec{v}_{ref} = \vec{V}_1 \cdot d_{V_1} + \vec{V}_2 \cdot d_{V_2} + \vec{0} \cdot d_{V_0} \tag{36}$$

These two duty cycles are combined with the duty cycles used to rebuild $\vec{V}_2$ from $\vec{V}_{00}$ and $\vec{V}_{10}$: $d_{V_{00}} = d_{V_{10}} = 1/2$

$$\vec{v}_{ref} = \vec{V}_{00} \cdot d_{V_1} + (\vec{V}_{00} \cdot d_{V_{00}} + \vec{V}_{10} \cdot d_{V_{10}}) \cdot d_{V_2} + \vec{0} \cdot d_{V_0} \tag{36}$$

$$\vec{v}_{ref} = \vec{V}_{00} \cdot (d_{V_1} + d_{V_{00}} \cdot d_{V_2}) + \vec{V}_{10} \cdot d_{V_{10}} \cdot d_{V_2} + \vec{0} \cdot d_{V_0} \tag{37}$$

Thus, the global duty cycles for the vectors $\vec{V}_{00}$ and $\vec{V}_{10}$ result in

$$D_{V_{00}} = d_{V_1} + d_{V_{00}} \cdot d_{V_2} = d_{V_1} + \frac{1}{2} \cdot d_{V_2} \tag{37}$$

$$D_{V_{10}} = d_{V_{10}} \cdot d_{V_2} = \frac{1}{2} \cdot d_{V_2} \tag{38}$$

The duty cycle of the zero vector is

$$D_{V_0} = 1 - D_{V_{00}} - D_{V_{10}}. \tag{39}$$

This vector can be obtained by using two opposite vectors during 50% d_{V_0} each one [9][10]. The result is similar for Sectors I, III, IV, VI and different for Sectors II and V since these two sectors are not limited by $\vec{V}_{00}$ or $\vec{V}_{11}$.

Unfortunately, the capacitor voltages are not constant so the magnitude and angle of $\vec{V}_{00}, \vec{V}_{01}, \vec{V}_{10}$ and $\vec{V}_{11}$ change over time and the value of the effective V_{dc} for the SVM after the fault is the minimum between $vc1$ and $vc2$. This issue can be overcome by recalculating the duty cycles in every program

cycle which keeps $\vec{V}_2, \vec{V}_3, \vec{V}_5$, and $\vec{V}_6$ located at exactly 60^0, $120^0, 240^0$ and 300^0 respectively. The global duty cycles that rebuild the hexagon $(\vec{V}_1, \vec{V}_2, \vec{V}_3, \vec{V}_4, \vec{V}_5, \vec{V}_6)$ from the four available space vectors $(\vec{V}_{00}, \vec{V}_{01}, \vec{V}_{10}, \vec{V}_{11})$ are shown in Table 6 [8].

Table 6 Duty cycles when $vc1 \neq vc2$

$a = \left(\frac{vc1 - vc2}{V_{dc}}\right)$	$vc2 \leq vc1$	$vc2 > vc1$
$\vec{V}_1$	$d_{V00} = 1$	$d_{V10} = \frac{vc1}{vc2}$
$\vec{V}_2$	$d_{V00} = \frac{1}{2}\cdot(1+a)$ $d_{V10} = \frac{vc2}{V_{dc}}$	$d_{V00} = \frac{1}{2}\cdot\left(\frac{vc1}{vc2}\right)\cdot(1+a)$ $d_{V10} = \frac{vc1}{V_{dc}}$
$\vec{V}_3$	$d_{V10} = \frac{vc2}{V_{dc}}$ $d_{V11} = \frac{1}{2}\cdot\left(\frac{vc2}{vc1}\right)\cdot(1-a)$	$d_{V10} = \frac{vc1}{V_{dc}}$ $d_{V11} = \frac{1}{2}\cdot(1-a)$
$\vec{V}_4$	$d_{V11} = \frac{vc2}{vc1}$	$d_{V11} = 1$
$\vec{V}_5$	$d_{V11} = \left(\frac{vc2}{2\cdot vc1}\right)\cdot(1-a)$ $d_{V01} = \frac{vc2}{V_{dc}}$	$d_{V11} = \frac{1}{2}\cdot(1-a)$ $d_{V01} = \frac{vc1}{V_{dc}}$
$\vec{V}_6$	$d_{V01} = \frac{vc2}{V_{dc}}$ $d_{V00} = \frac{1}{2}\cdot(1+a)$	$d_{V01} = \frac{vc1}{V_{dc}}$ $d_{V00} = \frac{1}{2}\cdot\left(\frac{vc1}{vc2}\right)\cdot(1+a)$

4.4. Suppression of the capacitor average voltage deviations

The DC offset voltage in the MSC and the GSC is controlled using the system presented in [22], Fig. 8. It prevents the average voltage in any of the capacitors from a slow and uncontrolled increase, which could be potentially destructive for them. Specifically, the fast and wide variations of power that characterizes the wave energy is a big challenge to the DC offset control system.
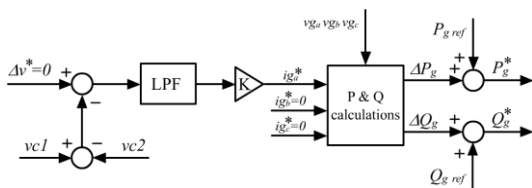
Fig. 8. *Voltage offset control used to suppress the deviations in the average DC voltage in capacitors*

4.5. Block diagram

The strategies to control an OWC WEC is a matter largely studied in the literature [23][11]. One of the strategies commonly admitted as adequate is based on the generation of a load torque proportional to the square of the rotor speed to avoid the need to periodically evaluate the sea state [23] (to set numerical values for the parameters appearing in the control equations)

$$T_{ref} = k \cdot \omega_r^2 \qquad (\omega < \omega_{limit}) \tag{13}$$

The MPC of the MSC uses this reference, in Fig. 9, to control the PMSG torque through i_{sq}

$$T_e = \frac{3}{2}p\lambda_f i_{sq} = T_{ref} \tag{14}$$

The magnetic field in the generator must be constant and therefore the i_{sd}^* command is usually zero except if the rotor speed exceeds its rated value, when would be necessary a field weakening.

The GSC control is shown in Fig. 10. In the GSC all the incoming power to the DC bus must be delivered to the grid in order to keep the DC voltage constant whereas the reactive power command, Q_g^*, is usually kept to zero unless the System Operator requires otherwise.
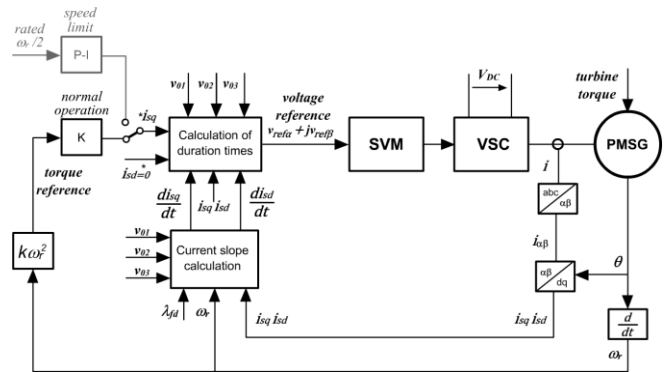
Fig. 9. *Block diagram of the MSC control system*
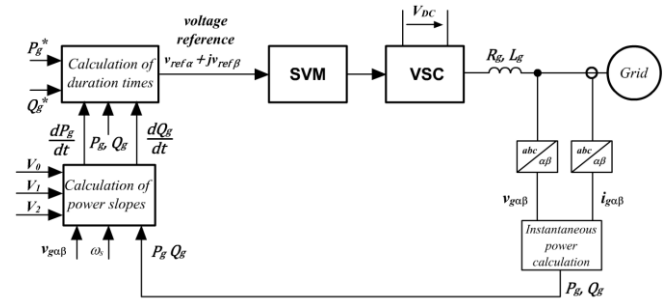
Fig. 10. *Block diagram of the GSC control system*

5. Experimental results

The proposed robust control for floating OWC WECs was tested in the laboratory using a scale emulator, Fig. 11.
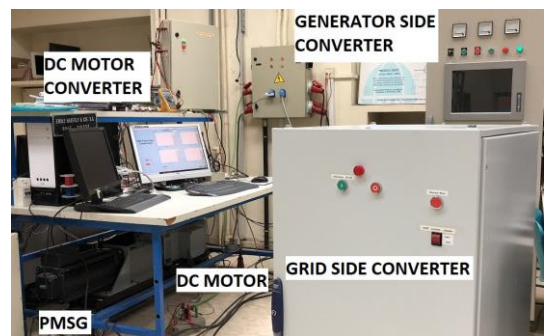
Fig. 11. *Photography of the OWC WEC emulator (DC motor, PMSG, and DC/DC converter), generator side converter (MSC), and GSC. The grid connection filter and step-up transformer are not visible*

The emulator is programmed with the OWC model presented in Section 2 and consists of a separately excited DC motor that reproduces the turbine torque, and a PMSG. A DC/DC power converter controls the DC motor according to Eq. (61) using a hysteresis band-based control, Fig. 12. The MSC and GSC are standard VSCs where one of the arms is disconnected from the grid or stator and connected to the midpoint of each DC link. The control was programmed in three dual-core floating point microcontrollers (MCU). The details of this emulator can be obtained in [24]. The line to line grid voltage was 230V for normal operation and 150V after a GSC fault while $V_{DC} = 500V$ in both cases.
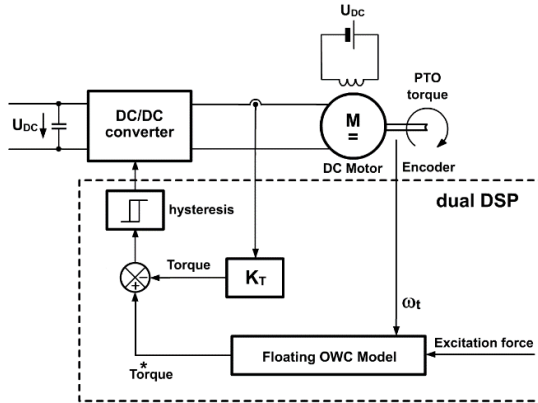
Fig. 12. *Block diagram of the OWC WEC emulator*

The following figures show, in red, the results obtained for each type of fault, and in blue or thin line, the corresponding results obtained in absence of fault in blue.

5.1. Fault in the GSC

In this case, the new configuration of the GSC during the fault limits the power that can be extracted from OWC WEC. The power limits used in the experimental tests are represented in Fig. 13 where an unfavorable case where absorbing reactive power is necessary was reproduced to better show this issue. The allowed operation area shows that it is necessary to absorb reactive power to make it possible delivering active power to the grid, and its limit is maximized for Q=-600var
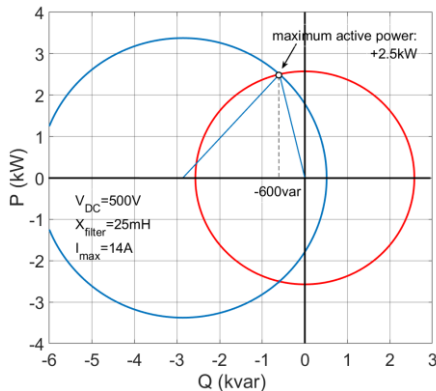
Fig. 13. *Power diagram after the fault (right).*

Once the open switch fault takes place, the power that the GSC is capable to handle decreases and, therefore, the relief valve in the air chamber must be opened. During the experimental tests, the relative pressure in the air chamber was limited to $0.7 \cdot \Psi$ from t=33s onwards. In consequence, the torque and power generated by the Wells turbine decreases, as illustrated in Fig. 14, and Fig. 15, respectively.

Due to the reduction of torque, the resulting PTO (rotor and turbine) rotating speed is lower compared to the pre-fault one, Fig. 16. Likewise, once the relief valve is opened, the power handled by the MSC is half the pre-fault one, Fig. 17. The key point is that the OWC WEC keeps delivering a significative amount of active power to the grid after the fault, Fig. 19. It must be noted that the GSC was absorbing a reactive power of Q=−600var at the same time, to improve its active power capability.
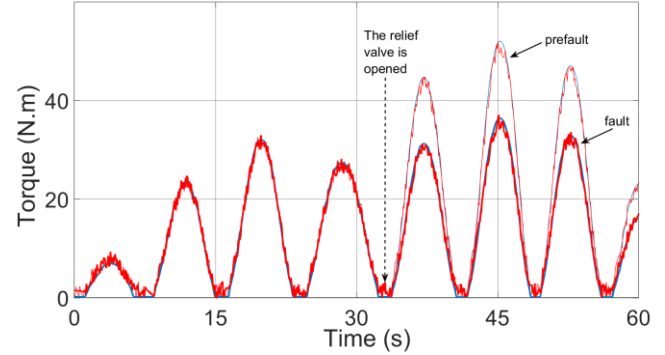
Fig. 14. *Wells turbine torque during the grid fault*
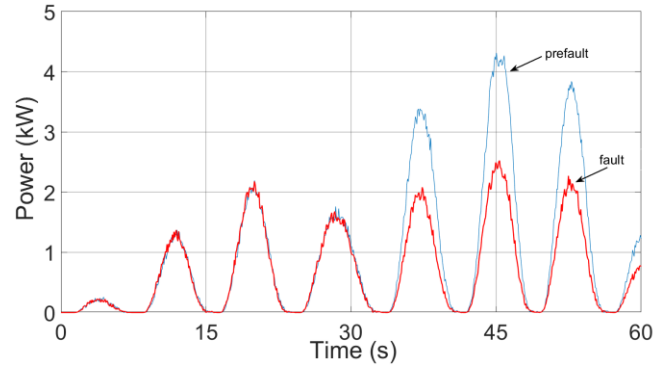
Fig. 15. *OWC WEC output power during the GSC fault*
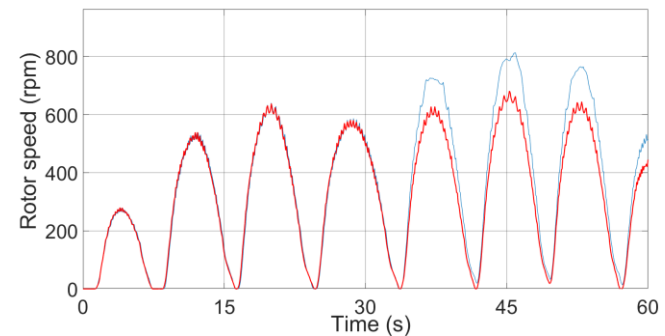
Fig. 16. *Wells turbine and PMSG speed during the GSC fault*
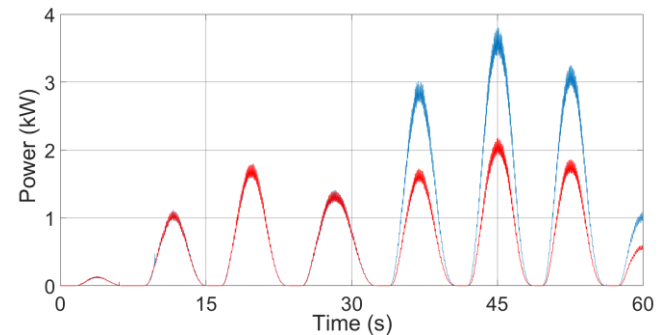
Fig. 17. *Power delivered by the PMSG during a fault in the GSC*

8
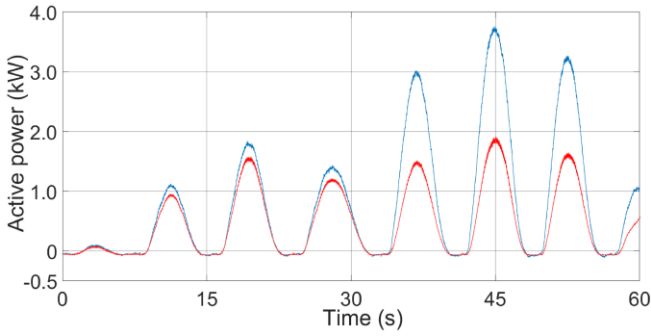
Fig. 19. *Active power delivered to the grid during the GSC fault*

Finally, Fig. 18 shows the MSC and GSC phase currents. Note that the GSC keeps a constant peak value due to the reactive power absorption that increases in some intervals, when, in addition, it handles active power.
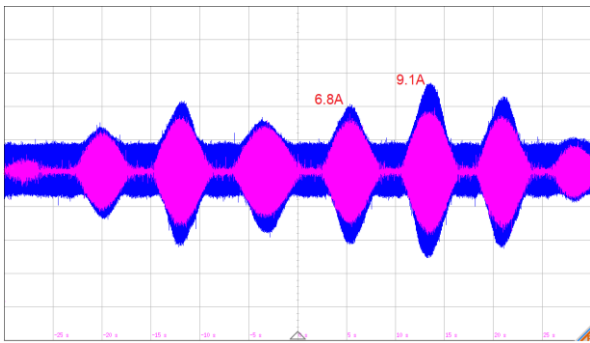
Fig. 18. *MSC (pink) and GSC (blue) currents during the GSC fault*

5.2. Fault in the MSC

The MSC rated power is approximately reduced to 50% of its original value when an open switch fault takes place. Thus, in this case it is also necessary to open the relief valve located in the air chamber to reduce the OWC WEC power. As in the GSC fault case, the relative pressure in the air chamber, was limited to $0.7 \cdot \Psi$ a t=33s onwards. Even so, if the rotor speed reaches half the rated rotor speed (500rpm), the MSC must limit that speed to prevent the e.m.f. from reaching the MSC maximum output voltage.

The Wells turbine torque is the same as in the case of the GSC fault, Fig. 14. However, the resulting output power is lower, compare Fig. 20 against Fig. 15, since the rotor speed is now lower, compare Fig. 21 against Fig. 16 and note how the speed control has kept it below around 500rpm. Consequently, the power handled by the MSC is also lower, Fig. 22 against Fig. 17, and the same happens to the active power delivered to the grid, Fig. 23.
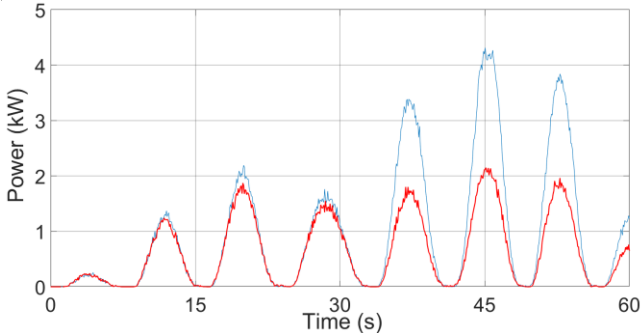
Fig. 20. *OWC WEC output power during the MSC fault (red)*
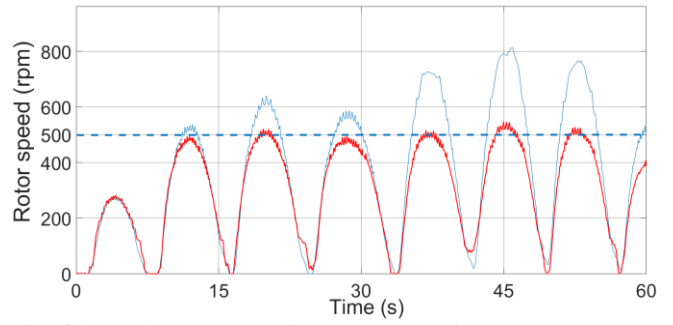
Fig. 21. *Wells turbine and PMSG speed during the MSC fault (red)*
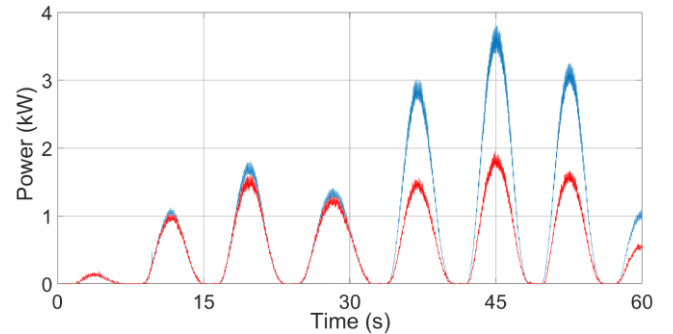
Fig. 22. *Power delivered by the PMSG during a fault in the MSC*
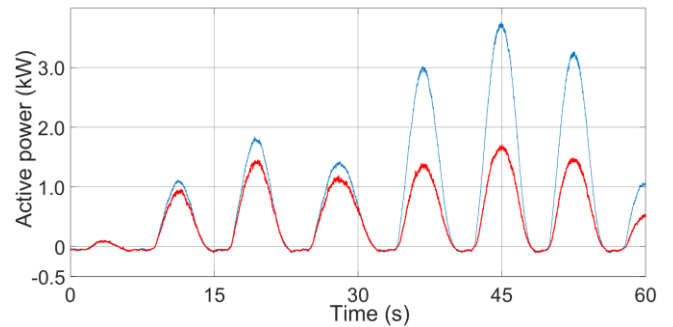
Fig. 23. *Active power delivered by the GSC to the grid during the MSC fault*

Fig. 24 shows the phase current in MSC and GSC, that in this case correspond to only active power since there is no fault in the GSC.
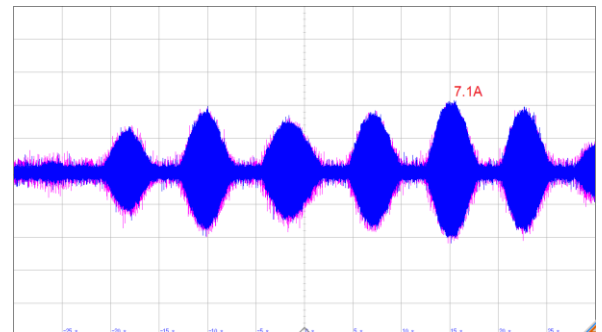
Fig. 24. *MSC (pink) and GSC (blue) currents during the MSC fault*

Finally, Fig. 25 shows the result obtained by the voltage offset control used to suppress deviations in the average DC voltage in the capacitors of the MSC. The result in the

9

capacitors of the GSC is similar. It must be noted that the DC offset suppression algorithm can lead to a slight waveform distortion if the duration times of the SVM come to be severely modified.
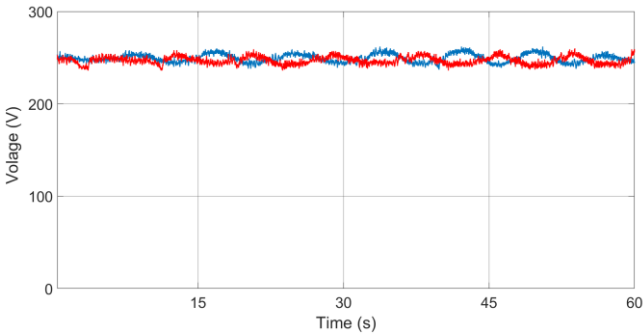
Fig. 25. *Voltage in the capacitors connected to the midpoint of the MSC DC link during the fault in the MSC*

5.3. Fault in the MSC and in the GSC

In the double fault case, the torque provided by the Wells turbine emulator and the corresponding rotor speed are the same as those of the MSC fault case. In effect, in both cases the relief valve is partially open to reduce the power and the rotor speed is limited to 500rpm. Consequently, the OWC output power, Fig. 26, is the same, and also the MSC output power, Fig. 27, and the active power delivered by the GSC, Fig. 29. However, like in the GSC fault case, it is necessary to absorb reactive power from the grid in order to increase the active power handling capacity and this is the reason because the grid current in Fig. 28 is higher than that of the Fig. 25. This current is also lower than that of the Fig. 18 since, for the same Wells turbine torque, the rotor speed is lower (limited to 500rpm by the MSC).
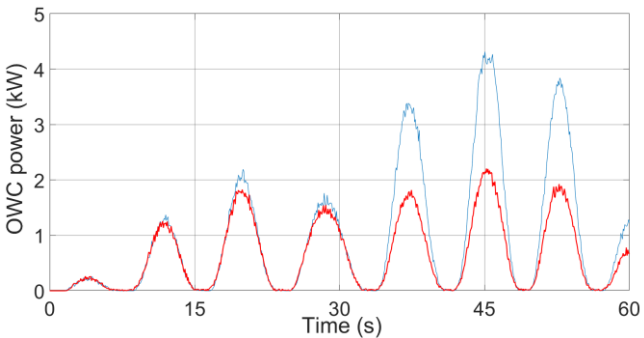
Fig. 26. *OWC WEC output power during the double fault*
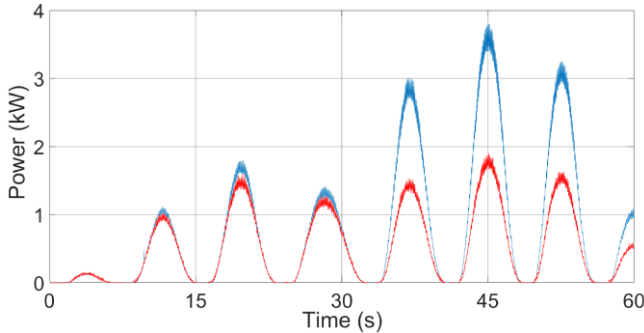
Fig. 27. *MSC power during the double fault (red)*
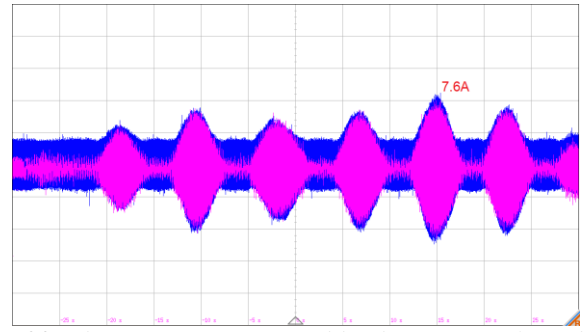
Fig. 28. *Phase current generated by the MSC (pink) and the GSC (blue) during the double fault*
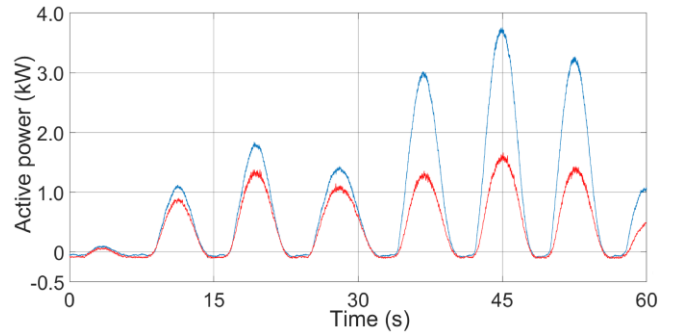
Fig. 29. *GSC power during the double fault (red)*

Finally, the MSC and GSC phase currents during the double fault are shown in Fig. 30 and Fig. 31 respectively.
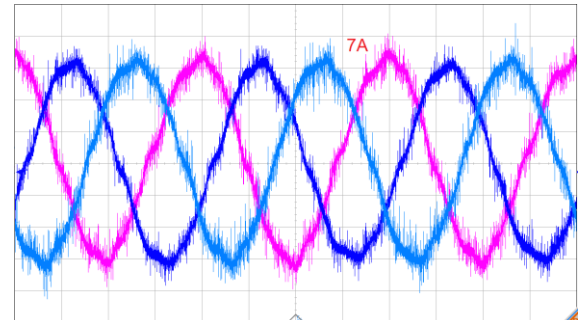
Fig. 30. *MSC phase current during the double fault. Switching frequency: 4kHz*
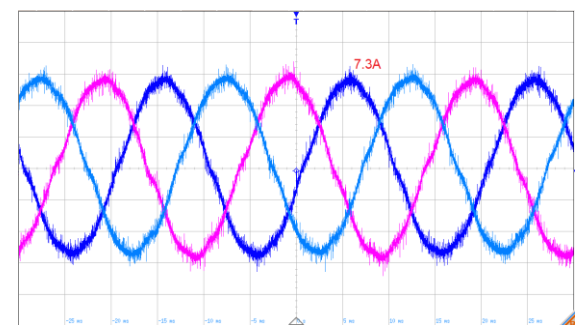
Fig. 31. *GSC phase current during the double fault. Switching frequency: 5kHz*

6. Conclusions

This paper presents a new robust control for a floating OWC WEC that can enable continuous operation even after an open switch fault takes place in one or two IGBTs of the MSC and/or the GSC. The configuration of the VSCs after each type of fault imposes certain limitations of power,

10

rotation speed and current that have been discussed, as well as the control of the relief valve in the air chamber. The control of both VSCs is an MPC adapted to use the four remaining space vectors available after each type of fault. The used modulation rebuilds the original hexagon from these vectors and combines two modulation schemes to generate the reference voltage vector.

The paper shows that the allowed peak power after the open switch fault is around 50% of the pre-fault peak. However, due to the power-time area (energy) below 50% is bigger than that over this limit, the energy harvested and delivered to the grid is bigger than 50% with respect to the pre-fault state. The tradeoff is that it is necessary to make some modifications to the original hardware such as adding three TRIACs to connect the faulty phase to the midpoint of the DC link, using a reduced AC grid, for example using a tapped transformer in the grid connection or alternatively increasing the DC link voltage, or overrating the IGBT current and transformer windings.

Therefore, with a moderate investment, it is possible to obtain a continuous operation of a floating OWC which can deliver energy to the grid even after certain types of faults in the VSCs, avoiding its grid disconnection and making the reparation less urgent. In fact, this increase in cost could be canceled out by the savings in maintenance tasks and by the revenues produced when, during a fault, it keeps delivering energy to the grid instead of getting disconnected.

7. References

[1] S. Faulstich, B. Hahn, and P. J. Tavner, "Wind turbine downtime and its importance for offshore deployment," *Wind Energy*, vol. 14, no. 3, pp. 327–337, Apr. 2011.

[2] P. Johannesson *et al.*, "Reliability Guidance for Marine Energy Converters," 2016.

[3] I. Garrido, A. J. Garrido, J. Lekube, E. Otaola, and E. Carrascal, "Oscillating water column control and monitoring," in *OCEANS 2016 MTS/IEEE Monterey*, 2016, pp. 1–6.

[4] H. Schulte and E. Gauterin, "Input-to-State Stability Condition for Passive Fault-Tolerant Control of Wave and Wind Energy Converters," *IFAC-PapersOnLine*, vol. 48, no. 21, pp. 257–262, 2015.

[5] M. Blanke and J. Schröder, *Diagnosis and fault-tolerant control*. Springer, 2006.

[6] Tian-Hua Liu, Jen-Ren Fu, and T. A. Lipo, "A strategy for improving reliability of field-oriented controlled induction motor drives," *IEEE Trans. Ind. Appl.*, vol. 29, no. 5, pp. 910–918, 1993.

[7] H.-C. Yu, C.-K. Lin, Y.-S. Lai, J. -t. Yu, and C.-I. Peng, "Two-vector-based modeless predictive current control for four-switch inverter-fed synchronous reluctance motors emulating the six-switch inverter operation," *Electron. Lett.*, vol. 52, no. 14, pp. 1244–1246, Jul. 2016.

[8] M. E. Zarei, M. Gupta, D. Ramirez, and F. Martinez-Rodrigo, "Switch Fault Tolerant Model-based Predictive Control (MPC) of a VSC Connected to the Grid," *IEEE J. Emerg. Sel. Top. Power Electron.*, 2019.

[9] K. Ni, Y. Hu, D. T. Lagos, G. Chen, Z. Wang, and X. Li, "Highly Reliable Back-to-Back Power Converter Without Redundant Bridge Arm for Doubly Fed Induction Generator-Based Wind Turbine," *IEEE Trans. Ind. Appl.*, vol. 55, no. 3, pp. 3024–3036, May 2019.

[10] K. Ni, Y. Hu, G. Chen, C. Gan, and X. Li, "Fault-Tolerant Operation of DFIG-WT With Four-Switch Three-Phase Grid-Side Converter by Using Simplified SVPWM Technique and Compensation Schemes," *IEEE Trans. Ind. Appl.*, vol. 55, no. 1, pp. 659–669, Jan. 2019.

[11] H. Bailey, B. R. D. Robertson, and B. J. Buckham, "Wave-to-wire simulation of a floating oscillating water column wave energy converter," *Ocean Eng.*, vol. 125, pp. 248–260, Oct. 2016.

[12] J. C. C. Henriques, L. M. C. Gato, A. F. O. Falcão, E. Robles, and F.-X. Faÿ, "Latching control of a floating oscillating-water-column wave energy converter," *Renew. Energy*, vol. 90, pp. 229–241, May 2016.

[13] J. C. C. C. C. Henriques, J. C. C. C. C. Portillo, L. M. C. M. C. Gato, R. P. F. P. F. Gomes, D. N. N. Ferreira, and A. F. O. F. O. Falcão, "Design of oscillating-water-column wave energy converters with an application to self-powered sensor buoys," *Energy*, vol. 112, pp. 852–867, Oct. 2016.

[14] J. Falnes, and M. Perlin, "Ocean Waves and Oscillating Systems: Linear Interactions Including Wave-Energy Extraction," *Appl. Mech. Rev.*, vol. 56, no. 1, pp. B3–B3, Jan. 2003.

[15] R. P. F. Gomes, J. C. C. Henriques, L. M. C. Gato, and A. F. O. Falcão, "Wave power extraction of a heaving floating oscillating water column in a wave channel," *Renew. Energy*, vol. 99, pp. 1262–1275, Dec. 2016.

[16] A. F. d. O. Falcão and P. A. P. Justino, "OWC wave energy devices with air flow control," *Ocean Eng.*, vol. 26, no. 12, pp. 1275–1295, Dec. 1999.

[17] K. Ni, Y. Hu, Y. Liu, and C. Gan, "Performance Analysis of a Four-Switch Three-Phase Grid-Side Converter with Modulation Simplification in a Doubly-Fed Induction Generator-Based Wind Turbine (DFIG-WT) with Different External Disturbances," *Energies*, vol. 10, no. 5, p. 706, May 2017.

[18] M. E. Zarei, D. Ramirez, C. V. Nicolas, and J. R. Arribas, "Three-Phase Four-Switch Converter for SPMS Generators Based on Model Predictive Current Control for Wave Energy Applications," *IEEE Trans. Power Electron.*, vol. 35, no. 1, pp. 289–302, Jan. 2020.

[19] T. Sun and S. Nielsen, "Semi-active feedforward control of a floating OWC point absorber for optimal power take-off," *IEEE Trans. Sustain. Energy*, pp. 1–1, 2019.

[20] M. E. Zarei, D. Ramirez, C. Veganzones, and J. Rodriguez, "Predictive Direct Control of SPMS Generators applied to the Machine Side Converter of an OWC power plant," *IEEE Trans. Power Electron.*, pp. 1–1, 2019.

[21] M. E. Zarei, C. V. Nicolas, J. R. Arribas, and D. Ramirez, "Four-Switch Three-Phase Operation of Grid-Side Converter of Doubly Fed Induction Generator With Three Vectors Predictive Direct

Power Control Strategy," *IEEE Trans. Ind. Electron.*, vol. 66, no. 10, pp. 7741–7752, Oct. 2019.

[22] K. Ni, Y. Hu, Y. Liu, and C. Gan, "Performance Analysis of a Four-Switch Three-Phase Grid-Side Converter with Modulation Simplification in a Doubly-Fed Induction Generator-Based Wind Turbine (DFIG-WT) with Different External Disturbances," *Energies*, vol. 10, no. 5, p. 706, May 2017.

[23] P. A. P. Justino, A. F. de O. Falca˜o, A. F. De, and O. Falc~o, *Rotational Speed Control of an OWC Wave Power Plant*, vol. 121, no. 2. American Society of Mechanical Engineers Digital Collection, 1999, pp. 65–70.

[24] D. Ramirez and G. Venkataramanan, "Development System for Wireless Control applied to Renewable Power Plants," *IEEE Trans. Sustain. Energy*, 2017.

8. Appendices

Table 1 OWC WEC model

OWC WEC Hydrodynamic force

ϱ_w	Sea water density
g	Gravity acceleration
$x_1(t)$	Position of the point absorber
$x_2(t)$	Position of the water column
S_1	Point absorber cross section
S_2	Chamber cross section
$F_{e,1}(t)$	Excitation force on the point absorber
$F_{e,2}(t)$	Excitation force on the water column
M_{11}^∞	Added mass at infinite frequency to the point absorber
$R_{r11}(t)$	Radiation resistance (damping) of the point absorber
M_{12}^∞	Added mass at mutual infinite frequency between point absorber and water column
$R_{r12}(t)$	Mutual radiation resistance (damping) between point absorber and water column
M_{22}^∞	Added mass at infinite frequency to the water column
$R_{r22}(t)$	Radiation resistance of the water column

Air Chamber/Wells turbine Power Take Off

F_{PTO}	Force generated by the PTO
p	Absolute pressure in the air chamber
p_0	Air pressure reference value
ρ_0	Air density reference value
p	Air pressure value
ρ	Air density value
Ψ	Relative pressure
Φ	Relative flow
γ	Isentropic exponent
N	Rotation speed
D	Diameter of the rotor
L_0	Air chamber height, $V_0 = L_0 \cdot S_2$

Table 2 OWC WEC dimensions

Radius of the air chamber	R_{Ch}=6.25m
Radius of the water column	R_{WC}=2.6m
Water column height	L_{WC}=6.0m
Turbine rotor diameter	D_R=2.1m
Distance between the water surface and the turbine	1.0m

Table 3 Space vectors available after open switch fault

S_b	S_c	$\vec{V}$	v_{an}	v_{bn}	v_{cn}	v_α	v_β
0	0	V_{00}	$\frac{2v_{c2}}{3}$	$-\frac{v_{c2}}{3}$	$-\frac{v_{c2}}{3}$	$\frac{2v_{c2}}{3}$	0
1	0	V_{10}	$\frac{v_{c2}-v_{c1}}{3}$	$\frac{2v_{c1}+v_{c2}}{3}$	$-\frac{v_{c1}+2v_{c2}}{3}$	$\frac{v_{c2}-v_{c1}}{3}$	$\frac{\sqrt{3}(v_{c1}+v_{c2})}{3}$
1	1	V_{11}	$-\frac{2v_{c1}}{3}$	$\frac{v_{c1}}{3}$	$\frac{v_{c1}}{3}$	$-\frac{2v_{c1}}{3}$	0
0	1	V_{01}	$\frac{v_{c2}-v_{c1}}{3}$	$-\frac{v_{c1}+2v_{c2}}{3}$	$\frac{2v_{c1}+v_{c2}}{3}$	$\frac{v_{c2}-v_{c1}}{3}$	$-\frac{\sqrt{3}(v_{c1}+v_{c2})}{3}$

Table 4 MPC of PMSG

v_{MSC}	Machine side converter voltage vector
v_s	Stator voltage vector
i_s	Stator current vector
λ_s	Stator flux
ω_r	Electrical rotor speed
R_s	Stator resistance
λ_f	Permanent magnet flux
L_s	Stator inductance
T_e	Electromagnetic torque
p	Number of pole pairs
i	Index of each space vector
S_i	Current slope
S_{da}, S_{db}, S_{dc}	Current slopes in the d axis
S_{qa}, S_{qb}, S_{qc}	Current slopes in the q axis
t_a, t_b, t_c	Duration times
T_s	Switching period

Table 5 MPC of GSC

v_{GSC}	Grid side converter voltage vector
v_g	Grid voltage vector
i_g	Grid phase current vector
L_f	Filter inductance
R_f	Filter resistance
P_g	Active power
Q_g	Reactive power
ω_s	Grid angular speed
S_{Pa}, S_{Pb}, S_{Pc}	Active power slopes
$S_{Qa}, S_{Qb}\ S_{Qc}$	Reactive power slopes
t_a, t_b, t_c	Duration times.
T_s	Switching period.